Chemical Science

ROYAL SOCIETY OF CHEMISTRY

EDGE ARTICLE

View Article Online
View Journal | View Issue

Cite this: *Chem. Sci.*, 2024, **15**, 9173

All publication charges for this article have been paid for by the Royal Society of Chemistry

Received 9th February 2024
Accepted 13th May 2024

DOI: 10.1039/d4sc00967c

rsc.li/chemical-science

Restructuring multi-phase interfaces from Cu-based metal–organic frameworks for selective electroreduction of CO_2 to C_2H_4†

Jiye Feng,[a] Wenbiao Zhang,[ab] Danni Shi,[a] Yingshuai Jia,[b] Yi Tang,[b] Yuying Meng[a] and Qingsheng Gao *[a]

Multi-phase interfaces are promising for surmounting the energy barriers of electrochemical CO_2 reduction involving multiple electron transfer steps, but challenges still remain in constructing interfacial microstructures and unraveling their dynamic changes and working mechanism. Herein, highly active Ag/Cu/Cu_2O heterostructures are *in situ* electrochemically restructured from Ag-incorporating HKUST-1, a Cu-based metal–organic framework (MOF), and accomplish efficient CO_2-to-C_2H_4 conversion with a high faradaic efficiency (57.2% at −1.3 V *vs.* RHE) and satisfactory stability in flow cells, performing among the best of recently reported MOFs and their derivatives. The combination of *in/ex situ* characterizations and theoretical calculations reveals that Ag plays a crucial role in stabilizing Cu(I) and increasing the CO surface coverage, while the active Cu/Cu_2O interfaces significantly reduce the energy barrier of C–C coupling toward the boosted ethylene production. This work not only proves MOFs as feasible precursors to derive efficient electrocatalysts on site, but also provides in-depth understanding on the working interfaces at an atomic level.

Introduction

The electrochemical CO_2 reduction reaction (CO_2RR) powered by renewable electricity provides a sustainable process toward carbon neutrality.[1,2] Compared with C_1 products (*e.g.*, CO, HCOOH, and CH_4), C_{2+} ones (*e.g.*, C_2H_4 and C_2H_5OH) feature higher energy density and market value; however, their productivity is seriously limited by the multi-step hydrogenation competing with a series of side-reactions.[3–5] So far, Cu is the only metal that can selectively convert CO_2 to C_{2+} thanks to the benign bonding of *CO intermediates,[6,7] and its interfaces with tailored valence states, grain boundaries and unsaturated sites are evidenced to surmount the energy barriers of such multiple electron transfer steps.[8–10] Although progress has been made in C_{2+} production, it's still challenging to facilely construct active interfaces and effectively stabilize them during electrolysis.[11]

Metal–organic frameworks (MOFs) have attracted extensive interest for the electrochemical CO_2RR associated with the high surface area, controllable pore size/shape, and open metal sites,[12–14] but as for the catalytic mechanism debates remain due to the dynamic change of frameworks during the tough electrolysis.[15] In particular, Cu-based MOFs containing frangible $Cu–O_4$ nodes would undergo *in situ* reconstruction since the electron transport along networks *via* the copper-ion redox demolishes the coordination extensively.[16] The newly formed surface/interfaces, rather than the initial frameworks, should be brought into sharp focus for the mechanism study.[17] Following the progressive insights, such electrochemical reconstruction was proved feasible to produce active and selective catalysts on site,[18–22] avoiding the time and energy-consuming preparation of catalysts and working electrodes (*e.g.*, thermally driven epitaxial growth of multi-phase interfaces[23,24] and ultrasonic spraying for loading powdery electrocatalysts onto gas-diffusion electrodes[25]). The *in situ* derived electrocatalysts inherit the structural merits of MOFs, and more importantly generate plenteous interfaces abundant with coordinatively unsaturated sites under the manipulated electrochemical conditions.[26] For example, the single-type Cu_2O sites of Cu_2O@CuHHTP and coordinatively unsaturated Cu paddle wheel clusters (Cu_2(-HCOO)$_3$), partially reduced from CuHHTP and HKUST-1 at mild potentials, promoted the selective CO_2RR to CH_4 in H-type reactors, while C_{2+} production was still restricted.[17,19] Moreover, the structure–activity relationship under working conditions was inconclusive in the context of the further reconfiguration at more negative potentials and higher current densities adopted for the CO_2RR, especially in flow cells. As

[a]*College of Chemistry and Materials Science, Guangdong Provincial Key Laboratory of Functional Supramolecular Coordination Materials and Applications, Jinan University, Guangzhou 510632, P. R. China. E-mail: tqsgao@jnu.edu.cn*

[b]*Department of Chemistry, Shanghai Key Laboratory of Molecular Catalysis and Innovative Materials, Laboratory of Advanced Materials, Collaborative Innovation Centre of Chemistry for Energy Materials, Fudan University, Shanghai 200433, P. R. China*

† Electronic supplementary information (ESI) available: Additional figures and data for CO_2RR performance, EDS mapping, additional XRD, IR, XPS and CVs, NMR spectra, XANES and EXAFS. See DOI: https://doi.org/10.1039/d4sc00967c

recently highlighted, the deep reconstruction of sulfur-doped HKUST-1 to ligand-free Cu/Cu_xS_y interfaces could enable efficient ethylene production;[18] however, such effort was hampered by the difficult control over the exchange of benzenetricarboxylic linkers by thioacetamide ligands in frangible frameworks. In other words, constructing, promoting and stabilizing interfacial active species, *e.g.*, Cu(0)–Cu(I) ensembles and defective sites, *via* elaborative MOF reconstruction are promising for robust C_{2+} production, but still an arduous task under the harsh CO_2RR conditions.[27,28]

Thanks to the thermodynamic merits of Ag in comparison with Cu, *e.g.*, the relatively higher standard redox potential ($E_{Ag^+/Ag}$ = +0.80 V *vs.* $E_{Cu^+/Cu}$ = +0.52 V) and the less negative formation enthalpy of oxides (−31.1 kJ mol^{-1} Ag_2O *vs.* −169 kJ mol^{-1} Cu_2O), introducing foreign Ag atoms is anticipated to stabilize neighboring Cu(I) active for the CO_2RR.[29] Moreover, it's also expected to empower tandem electrolysis on the expanded interfaces *via* available *CO spillover from weakly bonding Ag to Cu(0)–Cu(I) sites capable of C–C coupling.[30–32] However, the relevant research is still absent for directional MOF reconstruction. Here, Ag-incorporating HKUST-1 frameworks (Ag_n/HKUST-1, *n* denotes the molar ratio of Ag/Cu) were for the first time introduced to *in situ* restructure Ag/Cu/Cu_2O heterostructures under practical electrolysis conditions, which were highly active for CO_2-to-C_2H_4 conversion due to the rich Cu(I) species and Ag/Cu/Cu_2O interfaces. With an optimal loading of Ag (n_{Ag} : n_{Cu} = 0.1), the *in situ* derived electrocatalysts afforded a high C_2H_4 faradaic efficiency (FE) of 57.2% at −1.3 V *vs.* RHE, superior to those of HKUST-1 derivatives (17.4%), electro-deposited Ag/Cu/Cu_2O (16.7%), and their recently reported MOF-related counterparts, and maintained satisfactory long-term durability. The combination of *in*/*ex situ* characterizations and theoretical calculations confirmed that Ag played a crucial role in stabilizing Cu(I) and increasing CO surface coverage, while the resulting rich Cu/Cu_2O interface significantly reduces the energy barrier of C–C coupling toward boosted ethylene production.

Experimental section

Chemicals

Copper(II) nitrate trihydrate ($Cu(NO_3)_2 \cdot 3H_2O$, >99.0%), polyvinylpyrrolidone (PVP, MW 58 000) and *N*,*N*-dimethylformamide (DMF, 99.8%) were provided by Macklin Co., Ltd (Shanghai, China). 1,3,5-Benzenetricarboxylic acid (H_3BTC, 98%), potassium hydroxide (KOH, 85%) and silver nitrate ($AgNO_3$, 99.8%) were purchased from Aladdin Chemistry Co., Ltd (Shanghai, China). Nafion (5 wt%) solution was purchased from Sigma-Aldrich. Ethanol (99.7%) was bought from Sinopharm Chemical Reagent Co., Ltd. (Shanghai, China). All aqueous solutions were prepared using ultrapure water (>18 MΩ).

Material synthesis

Synthesis of HKUST-1. HKUST-1 was prepared *via* the reported method with a slight modification.[33] Typically, 8.6 mmol of $Cu(NO_3)_2 \cdot 3H_2O$ was dissolved in 15 mL of deionized water. A solution of H_3BTC acid (4.8 mmol) in a co-solvent of DMF and ethanol (30 mL, 1 : 1 by volume) was mixed with 2.0 g of PVP under continuous stirring. After complete dispersion of the reactants, the two solutions were mixed directly. Subsequently, the mixed solution was stirred for 15 min and transferred into a 50 mL Teflon-lined stainless-steel autoclave. The autoclave was heated at 100 °C for 10 h. After naturally cooling down to room temperature, the product was washed with ethanol three times by centrifugation at 8000 rpm for 5 min. Finally, the blue powder of HKUST-1 was obtained after drying under vacuum at 60 °C overnight.

Synthesis of Ag_n/HKUST-1. The $Ag_{0.1}$/HKUST-1 pre-catalyst was prepared by a wet chemistry method.[34] 5.4 mg (0.032 mmol) of $AgNO_3$ was dissolved in 10 mL of hydroalcoholic solution (V_{EtOH} : V_{H_2O} = 9 : 1), and then 70 mg (0.32 mmol) of the as-prepared HKUST-1 was added into the above solution with continuous stirring for 20 h at 85 °C. The precipitate was centrifuged, washed with ethanol and dried in a vacuum oven at 60 °C overnight. Furthermore, varied amounts of $AgNO_3$ were used to prepare Ag_n/HKUST-1 with different amounts of Ag incorporated.

Synthesis of EtOH reduced HKUST-1 (ER-HKUST-1). HKUST-1 was added to 10 mL of hydroalcoholic solution (V_{EtOH} : V_{H_2O} = 9 : 1) with continuous stirring for 20 h at 85 °C. The precipitate was centrifuged, washed with ethanol and dried in a vacuum oven at 60 °C overnight.

Physical characterization

Transmission electron microscopy (TEM), energy dispersive spectroscopy (EDS) and the corresponding elemental mapping were performed on a JEOL 2100F. Scanning electron microscopy (SEM) and energy dispersive spectroscopy (EDS) were conducted on a ZEISS ULTRA55. X-ray diffraction (XRD) analysis was performed on a Bruker D8 diffractometer using Cu Kα radiation (λ = 1.54056 Å). X-ray photoelectron and Auger electron spectroscopies (XPS and AES) were performed on a Thermo Scientific Escalab 250Xi. Fourier transform infrared (FT-IR) spectroscopy was carried out on a PerkinElmer spectrometer with the spectral range of 4000–400 cm^{-1}. Raman investigation was performed on a laser confocal Raman microspectrometer (Horiba HR-800) with an excitation laser wavelength of 532 nm. The electron paramagnetic resonance (EPR) spectra were recorded on a Bruker A300. Inductively coupled plasma-optical emission spectrometry (ICP-OES) analysis was conducted on an OPTIMA 2000DV. X-ray absorption spectroscopy (XAS) was performed at beamline 12-BM of the Advanced Photon Source beamline at Argonne National Laboratory in Illinois, USA.

Preparation of cathode electrodes

5 mg of electrocatalyst was ground to powder and then dispersed into anhydrous ethanol (450 μL) followed by adding 50 μL Nafion. After continuous ultrasonication for at least 30 min, a homogeneous ink was achieved. 100 μL of the ink was pipetted onto a carbon paper electrode (0.5 cm × 2 cm) with a loading of 1 mg cm^{-2}. The electrode was then dried at room temperature naturally for the subsequent electrochemical tests.

Electrochemical test

CO_2 electrolysis was performed in a flow cell. The prepared gas diffusion electrode (GDE) was the working electrode. An electrolyte (1.0 M KOH) was circulated through the flow cell at a rate of 15 mL min^{-1} under the pressure applied by a peristaltic pump. Anode and cathode chambers were separated by an anion exchange membrane. A platinum electrode and a solid Ag/AgCl electrode served as the counter electrode and reference electrode, respectively. Electrode potentials in the study were converted to the reversible hydrogen electrode (RHE) scale according to the following equation:

$$E_{(vs.\ \mathrm{RHE})} = E_{(vs.\ \mathrm{Ag/AgCl})} + 0.059 \times \mathrm{pH} + 0.197\ \mathrm{V}$$

All electrochemical measurements were carried out in a three-electrode system with a CHI660E potentiostat. Linear sweep voltammetry (LSV) curves were obtained to choose the appropriate potential range for the catalysts. The sweeping range was from 0 to −1.7 V (*vs.* RHE) at a scan rate of 100 mV s^{-1} in 1 M KOH solution with a CO_2 flow.

Products analysis

Gaseous products were analyzed using a gas chromatograph (GC, FULI-9790 II) equipped with a flame ionization detector (FID for CO and hydrocarbons) and a thermal conductivity detector (TCD for H_2). Gas-phase products were sampled every 20 min using high-purity nitrogen (N_2, 99.999%) as the carrier gas. The column effluent (separated gas mixtures) was first passed through the TCD where hydrogen was quantified, then CO, CH_4 and C_2H_4 were subsequently quantified by the FID. According to the peak areas in the GC, the partial current densities and FEs of CO, CH_4, C_2H_4 and H_2 were calculated using the following equations:

$$j_x = \frac{\text{peak area of } x}{\alpha} \times \text{flow rate} \times \frac{nF}{V_m} \times (\text{electrode area})^{-1}$$

$$\mathrm{FE} = \frac{j_x}{j_{\mathrm{total}}}$$

where x represents one of CO, CH_4, C_2H_4 and H_2, and n represents the number of electrons to be transferred to form the products, which are 2, 8, 12 and 2, respectively; α is the conversion factor for CO, CH_4, C_2H_4 and H_2, respectively, based on the calibration of standard samples; F is the Faraday constant ($F = 96\,485$ C mol^{-1}), and $V_m = 22.4$ L mol^{-1}.

The liquid products were quantified using ^1H nuclear magnetic resonance (NMR) (AVANCE III HD 400 MHz), in which 0.1 mL of the electrolyte was mixed with 0.5 mL of D_2O, and DMSO was used as an internal standard.

Theoretical calculations

DFT calculations were performed at the GGA level within the Perdew–Burke–Ernzerhof (PBE) functional using the CASTEP software implemented in Materials Studio. The total energy calculation was performed using a kinetic energy cutoff of 450.0 eV assigned to the plane-wave basis set for calculating the density of states. The self-consistent field (SCF) tolerance was 1×10^{-6} eV. The Brillouin zone was sampled using $5 \times 5 \times 1$ *k*-points. The core electrons were replaced with ultrasoft pseudopotentials. An fcc Cu model was used to further construct Cu–Ag and Cu–Cu_2O. The fcc Cu–Ag was constructed by replacing a Cu atom with Ag. Then, we selected a 3×3 relaxed rhombus $Cu_2O(001)$ bilayer on top of a relaxed 3×3 Cu(001) surface to model Cu/Cu_2O heterojunctions, in which O atoms were introduced to saturate the Cu atoms on the Cu(001) thus the surface atoms are well passivated. The Cu(100), Cu–Ag(100) and Cu–Cu_2O(100) surfaces were modeled using five layer slabs to study the CO_2 reduction activity. A vacuum region of 15 Å between any two repeated slabs was used to avoid interactions between repeated slabs along the *z*-direction.

The binding energy (BE) of an adsorbate was calculated as:

$$\mathrm{BE}_{(\mathrm{adsorbate})} = E_{(\mathrm{slab+adsorbate})} - E_{(\mathrm{slab})} - E_{(\mathrm{adsorbate})}$$

where $E_{(\mathrm{slab+adsorbate})}$, $E_{(\mathrm{slab})}$ and $E_{(\mathrm{adsorbate})}$ are the total energy of the slab with an adsorbate, the energy of the pure slab/facet and the energy of the adsorbate in the gas phase, respectively.

The Gibbs free energy (G) of a species was calculated as:

$$G = E + \mathrm{ZPE} - TS$$

where E is the total energy of a species obtained from DFT calculations, and ZPE and S are the zero-point energy and entropy of the species, respectively. A potential of 0 V was adopted in the calculation. The change in free energy (ΔG) was calculated as:

$$\Delta G = \Delta E + \Delta\mathrm{ZPE} - T\Delta S$$

The transition state search used complete LST/QST in 0.25 eV $Å^{-1}$ RMS convergence, with the optimized reactant and product geometries as starting points. CASTEP employed algorithms such as the nudged elastic band (NEB) or the dimer method to explore the potential energy surface and locate the transition state structure. The transition state was obtained between reactants and products while minimizing the energy in 10 QST steps.

Results and discussion

An HKUST-1 framework is built up of dimeric Cu units connected by benzene-1,3,5-tricarboxylate linkers. It was fabricated *via* a previously reported method,[33] and then was incorporated with Ag after reacting with $AgNO_3$ in a hydroalcoholic solution ($V_{EtOH} : V_{H_2O} = 9 : 1$), where EtOH was the reducing agent that reduced Ag(I) to metallic Ag and partially reduced Cu(II) to Cu(I).[34] Accordingly, we also prepared a reference sample *via* a similar process in the absence of $AgNO_3$, which was named EtOH reduced HKUST-1 (ER-HKUST-1).

The crystal structure of the as-prepared samples was analyzed by XRD (Fig. 1a). $Ag_{0.1}$/HKUST-1 presented

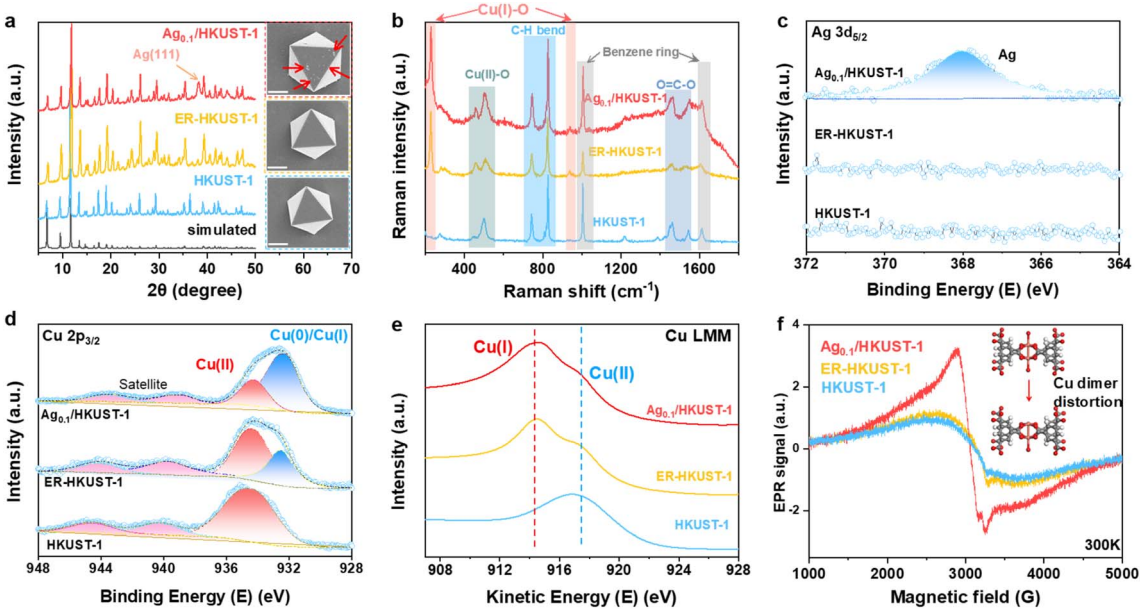

Fig. 1 Structural characterization of HKUST-1, ER-HKUST-1 and $Ag_{0.1}$/HKUST-1: (a) XRD patterns, (insets of a) SEM images with the scale bar of 1 μm, (b) Raman spectra, (c) high-resolution Ag $3d_{5/2}$ XPS, (d) high-resolution Cu $2p_{3/2}$ XPS, (e) Cu LMM AES and (f) EPR spectra.

a characteristic pattern consistent with those of HKUST-1 and ER-HKUST-1, confirming the well-retained framework after Ag loading and partial reduction. This is also supported by their same absorption bands in FT-IR spectra (Fig. S1, ESI†). A new peak of Ag(111) appearing in $Ag_{0.1}$/HKUST-1 indicated the successful loading of Ag. An identical octahedral structure was observed in the three samples by SEM (insets of Fig. 1a), and the small nanoparticles (marked by red arrows) on the surface of $Ag_{0.1}$/HKUST-1 should be assigned to the incorporated Ag. Accordingly, the elemental mapping performed with both SEM and TEM revealed the uniform distribution of O, Cu and Ag elements over $Ag_{0.1}$/HKUST-1 octahedrons (Fig. S2, ESI†). In the Raman spectra (Fig. 1b), two new bands at 218 and 930 cm^{-1}, responsible for the Cu(I)–O vibrations,[34] appeared in ER-HKUST-1 and $Ag_{0.1}$/HKUST-1, which indicated the partial reduction of Cu(II) to Cu(I).

The chemical composition and element valence state were further studied by XPS and AES. Different from HKUST-1 and ER-HKUST-1, $Ag_{0.1}$/HKUST-1 displayed a broad Ag 3d peak at 368.1 eV in XPS (Fig. 1c), confirming the successful incorporation of Ag. In the profile of Cu $2p_{3/2}$, the peak at 934.5 eV was attributed to Cu(II) species, and that at 932.4 eV could be assigned to Cu(0) or Cu(I) (Fig. 1d).[18] AES with the good resolution of Cu(0)/Cu(I) further identified the co-presence of Cu(I) and Cu(II) in both $Ag_{0.1}$/HKUST-1 and ER-HKUST-1, in comparison with the dominant Cu(II) in HKUST-1 (Fig. 1e). Therefore, the peak at 932.4 eV in the Cu $2p_{3/2}$ XPS profile should be ascribed to the Cu(I) species in $Ag_{0.1}$/HKUST-1 and ER-HKUST-1, which was derived from the partial reduction of Cu(II) by EtOH. It's noteworthy that $Ag_{0.1}$/HKUST-1 showed a relatively higher intensity of Cu(I) in both XPS and AES profiles as compared with ER-HKUST-1, suggesting the stabilization of Cu(I) by additive Ag. The presence of Cu(I) would cause the distortion of the Cu–Cu dimer, as confirmed by the high signal intensity of $Ag_{0.1}$/HKUST-1 in EPR (Fig. 1f).[35] In addition, a series of Ag_n/HKUST-1 frameworks with an identical structure but different Ag/Cu molar ratios could be obtained after varying the feeding ratio (Fig. S3–S7, ESI†), which showed a volcano relationship between Cu(I)/Cu(II) and Ag/Cu ratios (Fig. S8, ESI†), indicating the enriched Cu(I) at a moderate Ag loading.

We conducted *in situ* Raman analysis combined with a CO_2RR test at various potentials to assess the reconstruction of such Cu-based MOFs (Fig. S9, ESI†). The bands corresponding to Cu(II)–O and C–H disappeared quickly at the applied bias, indicating the collapse of the metal–organic framework. The emerging band of Cu–CO further suggested the formation of *CO on the *in situ* formed metallic surface.[36] Of particular interest is the appearance of Cu_2O bands at 520 and 610 cm^{-1} in $Ag_{0.1}$/HKUST-1 and ER-HKUST-1 compared to HKUST-1,[37] whose intensity increased with the negative potentials and reached a maximum at −1.3 V *vs.* RHE. Thus, the *in situ* reconstruction of the three samples was further analyzed at −1.3 V *vs.* RHE in a flow cell. As the model sample, $Ag_{0.1}$/HKUST-1 afforded a fluctuating current density initially in chronoamperometry (Fig. 2a), which afterwards became more stable after 1 h electrolysis, suggesting that the reconfiguration can be completed within the first hour. To observe the reconstruction process more directly, the reconstituted samples were subjected to SEM (Fig. 2b–d). Obviously, the octahedral structure collapsed after only 1 min, and the final morphology of HKUST-1 and ER-HKUST-1 was granular, whereas $Ag_{0.1}$/HKUST-1 exhibited dendritic nanostructures that can obviously enhance surface hydrophobicity (Fig. S10, ESI†). As previously evidenced,[38,39] electrocatalysts with a hydrophobic surface would be favorable for the CO_2RR because of the inhibited hydrogen evolution competition. Interestingly, the reconfigured

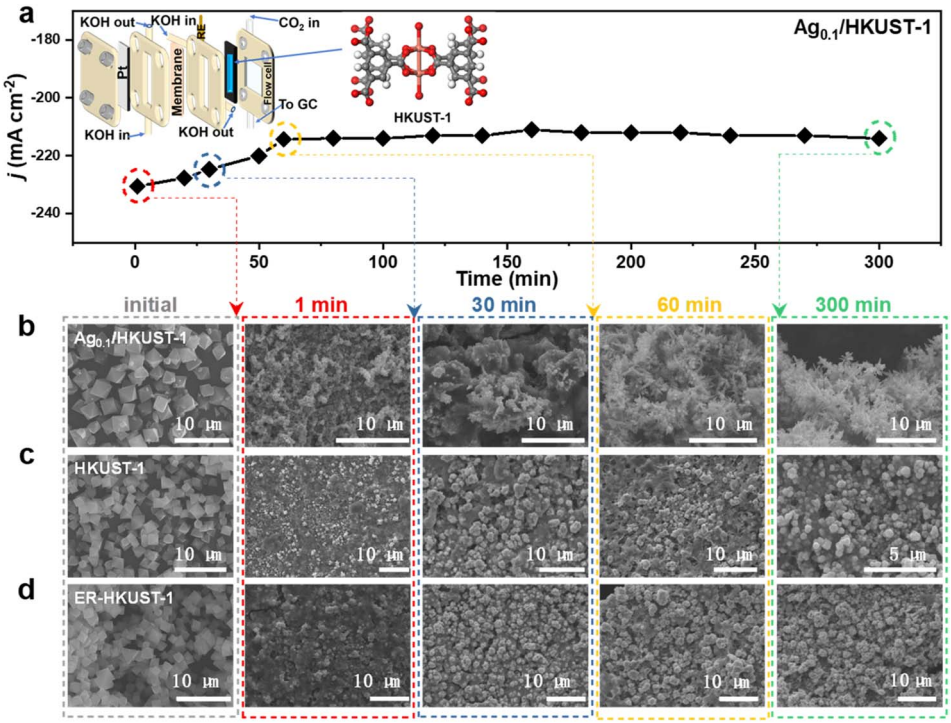

Fig. 2 (a) Chronoamperometry curve of $Ag_{0.1}$/HKUST-1 during *in situ* electrochemical reconstruction at −1.3 V *vs.* RHE, and SEM images of (b) $Ag_{0.1}$/HKUST-1, (c) HKUST-1 and (d) ER-HKUST-1 collected at 0, 1, 30, 60, and 300 min.

samples after 1 h and 5 h of electrolysis presented identical nanostructures, further confirming the rapid reconstruction finished within 1 h. Accordingly, the disappearance of the characteristic peaks of the benzene ring in FT-IR indicated that the organometallic framework has been drastically destroyed (Fig. S11, ESI†). This is distinct from the previous reports of ligand-retaining Cu surfaces (*e.g.*, Cu_2O@CuHHTP,[17] $Cu_2(HCOO)_3$ clusters,[19] PPy/HKUST-1,[21] and PANI/HKUST-1 (ref. 21)), and guarantees a reliable platform to unravel the structure–activity relationship of *in situ* formed interfaces.

The restructured electrocatalysts from HKUST-1, ER-HKUST-1 and $Ag_{0.1}$/HKUST-1 after 1 h of CO_2RR were denoted as $Cu_{HKUST-1}$, $Cu/Cu_2O_{ER\text{-}HKUST\text{-}1}$ and $Ag/Cu/Cu_2O_{Ag_{0.1}/HKUST\text{-}1}$, respectively. To minimize the impact of oxidation, the samples were immediately transferred to an argon-filled glovebox for further characterization. As depicted in their XRD patterns (Fig. 3a), the diffraction peaks of the original framework disappeared. Instead, typical peaks of Cu(111) and (200) were detected at $2\theta = 43.3°$ and 50.4°, respectively. Besides, the visible Cu_2O(111) and (200) in both $Cu/Cu_2O_{ER\text{-}HKUST\text{-}1}$ and $Ag/Cu/Cu_2O_{Ag_{0.1}/HKUST\text{-}1}$, and the Ag(111) and (200) in $Ag/Cu/Cu_2O_{Ag_{0.1}/HKUST\text{-}1}$ confirmed the co-presence of multiple phases, *i.e.*, Cu/Cu_2O and $Ag/Cu/Cu_2O$. In the Cu 2p XPS profiles (Fig. 3b), unlike the pre-catalysts, the peak of Cu(II) was absent in the reconstructed samples, and only the peak at 932.4 eV associated with Cu(0)/Cu(I) was observed, which indicated the reduction of Cu(II) at the applied potential. $Cu/Cu_2O_{ER\text{-}HKUST\text{-}1}$ and $Ag/Cu/Cu_2O_{Ag_{0.1}/HKUST\text{-}1}$ showed peaks at 914.3 and 917.3 eV in the AES, corresponding to Cu(I) and Cu(0) species,[40] while only Cu(0) was present on $Cu_{HKUST-1}$ (Fig. 3c), which were consistent with the XRD results. Compared to the pre-catalysts, the peak of Ag 3d on $Ag/Cu/Cu_2O_{Ag_{0.1}/HKUST\text{-}1}$ shifted toward a lower binding energy (Fig. S12, ESI†), probably due to Ag aggregation along with the electrochemical reconstruction.[41]

The high-resolution TEM (HR-TEM) image of $Ag/Cu/Cu_2O_{Ag_{0.1}/HKUST\text{-}1}$ clearly showed the interfaces of $Ag/Cu/Cu_2O$ (Fig. 3d). The lattice fringes of 0.181, 0.204 and 0.245 nm could be indexed to Cu(200), Cu(111) and Cu_2O(111), respectively, and those of 0.204 and 0.235 nm were assigned to

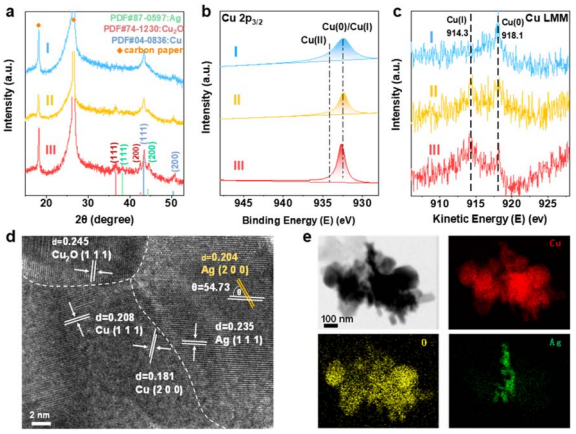

Fig. 3 (a) XRD patterns, (b) high-resolution Cu $2p_{3/2}$ XPS and (c) Cu LMM AES of (I) $Cu_{HKUST-1}$, (II) $Cu/Cu_2O_{ER\text{-}HKUST\text{-}1}$ and (III) $Ag/Cu/Cu_2O_{Ag_{0.1}/HKUST\text{-}1}$. (d) HR-TEM image and (e) elemental mapping of $Ag/Cu/Cu_2O_{Ag_{0.1}/HKUST\text{-}1}$.

Ag(200) and Ag(111). In comparison, the lattice planes of Cu(111) and Cu_2O(111) were visible in $Cu/Cu_2O_{ER\text{-}HKUST\text{-}1}$, and only Cu(111) was observed in $Cu_{HKUST\text{-}1}$ (Fig. S13, ESI†). In Fig. 3e, the elements of Cu and O were uniformly distributed throughout the nanostructures, while the concentrated distribution of Ag suggested the formation of an $Ag/Cu/Cu_2O$ multiphase with abundant interfaces, rather than Ag–Cu alloys.

Furthermore, the X-ray absorption near edge structure (XANES) and extended X-ray absorption fine structure (EXAFS) of $Ag/Cu/Cu_2O_{Ag_{0.1}HKUST\text{-}1}$ were analysed to understand the local environments of Ag and Cu (Fig. S14, ESI†). The Ag K-edge overlapped with that of Ag foil, indicating a close-to-zero valence state of Ag in $Ag/Cu/Cu_2O_{Ag_{0.1}HKUST\text{-}1}$. But the white line peak was slightly lower, consistent with the XPS data (Fig. S12, ESI†), which was probably due to the electron transfer from Cu to Ag. The electron transfer between Ag and Cu may lead to the formation of Ag–Cu bonds, as well as the existence of an Ag–Cu interface.[42] Accordingly, the Cu K-edge analysis presented a slightly higher valence state of Cu than that of the Cu_2O reference. Moreover, the k^2-weighted Ag K-edge EXAFS showed that the bond length and coordination number of Ag in $Ag/Cu/Cu_2O_{Ag_{0.1}HKUST\text{-}1}$ were slightly reduced, suggesting the formation of a heterostructure rather than alloys. Analogously, the increased Cu–O signal in the Cu K-edge EXAFS as compared with that of a Cu reference indicated the considerable amount of Cu_2O in the restructured interfaces, and the lower Cu–O coordination number and the accordingly longer Cu–O bond in comparison with those of a Cu_2O reference might be due to the presence of heterogeneous interfaces. In addition, wavelet transform analysis highlighted the dominance of Ag–Ag and Cu–O bonds in the heterostructures, while Ag–O and Cu–Cu bonds are negligible, matching well with the EXAFS fitting results (Fig. S15 and Table S1, ESI†).

The electrochemical CO_2RR performance of $Cu_{HKUST\text{-}1}$, $Cu/Cu_2O_{ER\text{-}HKUST\text{-}1}$ and $Ag/Cu/Cu_2O_{Ag_{0.1}/HKUST\text{-}1}$ was evaluated in a flow cell with 1.0 M KOH as the electrolyte. The polarization curves showed the highest current densities of $Ag/Cu/Cu_2O_{Ag_{0.1}/HKUST\text{-}1}$ among the three samples (Fig. 4a), indicative of the high activity of the restructured $Ag/Cu/Cu_2O$. The electrolyte after reaction was analyzed by using ^1H nuclear magnetic resonance (NMR) spectroscopy, which suggested the negligible formation of liquid products (Fig. S16, ESI†). As evidenced by recent reports,[38,43] the higher coverage and transport efficiency of chemisorbed *H derived from abundant H_2O on gas–liquid–solid interfaces would benefit the generation of alcohols, the typical liquid products of the CO_2RR. Herein, the superhydrophobic surface of the restructured $Ag/Cu/Cu_2O$ (Fig. S10, ESI†) probably prohibits the formation of alcohol products. With further regard to the same key step of *CO coupling shared by ethylene and ethanol formation, we thereby focused on the gas products quantified by on-line GC for the understanding of the restructured interfaces, to avoid the superposition of instrumental errors (*e.g.*, GC and NMR). Potentiostatic measurements at −1.0 to −1.5 V (*vs.* RHE) showed that Ag/Cu/

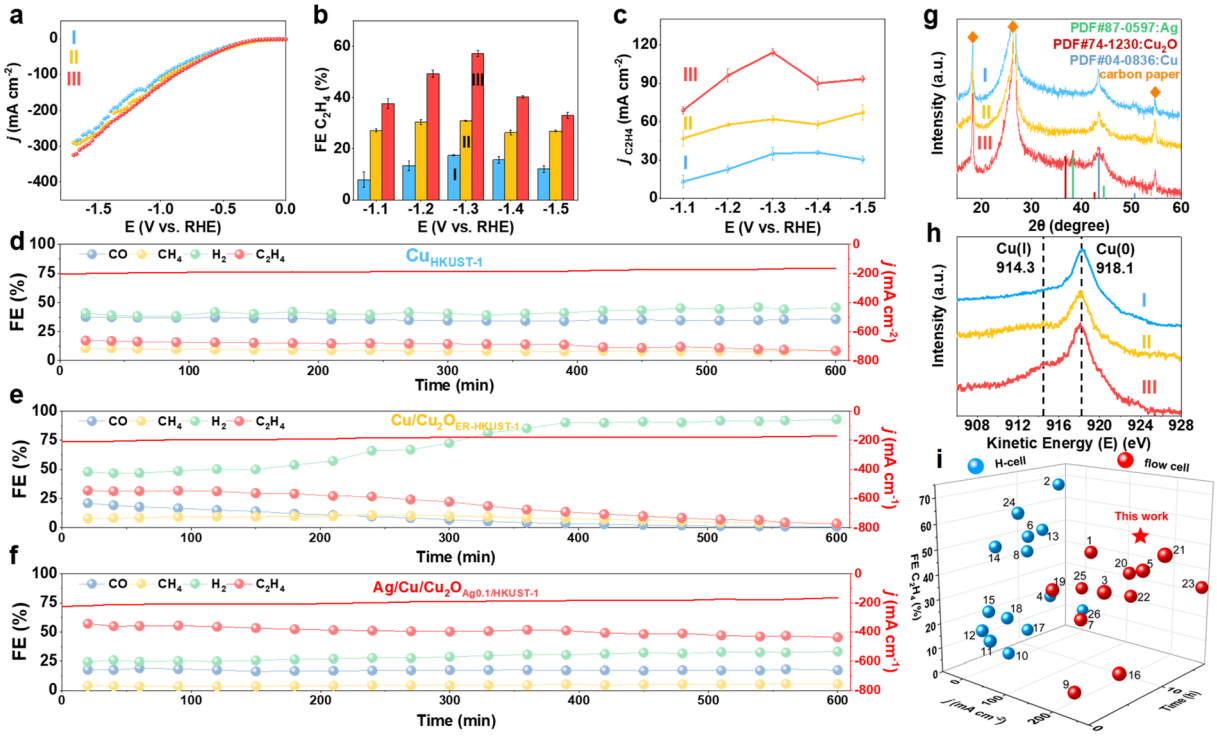

Fig. 4 (a) Polarization curves, (b) FE and (c) partial current density of C_2H_4 at different applied potentials of (I) $Cu_{HKUST\text{-}1}$, (II) $Cu/Cu_2O_{ER\text{-}HKUST\text{-}1}$ and (III) $Ag/Cu/Cu_2O_{Ag_{0.1}/HKUST\text{-}1}$ in CO_2-saturated 1.0 M KOH. Chronoamperometric stability tests of (d) $Cu_{HKUST\text{-}1}$, (e) $Cu/Cu_2O_{ER\text{-}HKUST\text{-}1}$ and (f) $Ag/Cu/Cu_2O_{Ag_{0.1}/HKUST\text{-}1}$. (g) XRD patterns and (h) Cu LMM AES of $Cu_{HKUST\text{-}1}$, $Cu/Cu_2O_{ER\text{-}HKUST\text{-}1}$ and $Ag/Cu/Cu_2O_{Ag_{0.1}/HKUST\text{-}1}$ after the CO_2RR (600 min). (i) Performance of $Ag/Cu/Cu_2O_{Ag_{0.1}/HKUST\text{-}1}$ compared with the recently reported Cu-based electrocatalysts (the numbers of reference samples are obtained from Table S2, ESI†).[16,18–20,35,44–64]

$Cu_2O_{Ag_{0.1}/HKUST\text{-}1}$ produced mainly C_2H_4 with the maximum FE of 57.2% at −1.3 V *vs.* RHE, while this value was only 17.4% on $Cu_{HKUST\text{-}1}$ (Fig. 4b). The reaction profiles of $Cu_{HKUST\text{-}1}$, $Cu/Cu_2O_{ER\text{-}HKUST\text{-}1}$ and $Ag/Cu/Cu_2O_{Ag_{0.1}/HKUST\text{-}1}$, including product FEs and current densities, are depicted in Fig. S17, ESI.† Accordingly, $Ag/Cu/Cu_2O_{Ag_{0.1}/HKUST\text{-}1}$ afforded a higher partial current density of C_2H_4 ($j_{C_2H_4}$) than $Cu_{HKUST\text{-}1}$ and $Cu_{ER\text{-}HKUST\text{-}1}$ (Fig. 4c), confirming the promoted ethylene production over Ag/Cu/Cu_2O heterostructures. For comparison, either the reference sample consisting of physically mixed Cu, Ag and Cu_2O nanoparticles or the electro-deposited one delivered a lower FE of C_2H_4 than $Ag/Cu/Cu_2O_{Ag_{0.1}/HKUST\text{-}1}$ under the same conditions (Fig. S18, ESI†), which highlighted the key contribution of MOF precursors to construct active Ag/Cu/Cu_2O multi-interfaces. To further unravel the effect of Ag, the CO_2RR performance of a series of Ag/Cu/Cu_2O derived from Ag_n/HKUST-1 frameworks was measured (Fig. S19, ESI†). With the increase of Ag content, the FE of C_2H_4 gradually increased and then tended to decrease, which indicated the benefited synergy of active components on the *in situ* generated Ag/Cu/Cu_2O interfaces with an optimal composition.

The electrochemically active surface area (ECSA) of the catalysts could be evaluated in terms of double-layer capacitance (C_{dl}, Fig. S20, ESI†), on the basis of their proportional correlation. $Ag/Cu/Cu_2O_{Ag_{0.1}/HKUST\text{-}1}$ presented a C_{dl} value of 3.24 mF cm^{-2}, exceeding those of $Cu_{ER\text{-}HKUST\text{-}1}$ (2.68 mF cm^{-2}) and $Cu/Cu_2O_{HKUST\text{-}1}$ (2.04 mF cm^{-2}), which indicated enriched active-sites after restructuring Ag/Cu/Cu_2O multi-interfaces. Meanwhile, electrochemical impedance spectroscopy (EIS) pointed out the relatively smaller electron-transfer resistance (R_{ct}) on $Ag/Cu/Cu_2O_{Ag_{0.1}/HKUST\text{-}1}$ (Fig. S21, ESI†), in good accordance with its higher activity.

The long-term stability was evaluated by conducting a chronoamperometric test (Fig. 4d–f). On $Cu_{HKUST\text{-}1}$, the main products were H_2 and CO with FEs of ∼40% and ∼35%, respectively, and the FE of C_2H_4 was lower than 18%. Although the C_2H_4 production was impressively enhanced on $Cu_{ER\text{-}HKUST\text{-}1}$ ($FE_{C_2H_4}$ ∼30%) during the initial reaction, it suffered from a drastic decrease to <20% after 300 min, concomitant with the increase of H_2 production. In sharp comparison, $Ag/Cu/Cu_2O_{Ag_{0.1}/HKUST\text{-}1}$ manifested a remarkably stable FE of C_2H_4 (∼50%) within 600 min, which should be ascribed to the Ag additives. In addition, compared to $Cu_{HKUST\text{-}1}$, $Cu/Cu_2O_{ER\text{-}HKUST\text{-}1}$ and $Ag/Cu/Cu_2O_{Ag_{0.1}/HKUST\text{-}1}$ showed a significantly lower CO yield and higher C_2H_4 yield during the initial reactions, which was accounted for by the effective consumption of *CO to produce C_2H_4. Afterwards, the CO production suffered a continuous decrease on $Cu/Cu_2O_{ER\text{-}HKUST\text{-}1}$, whereas it was almost constant on $Ag/Cu/Cu_2O_{Ag_{0.1}/HKUST\text{-}1}$, suggesting a dynamic balance of *CO formation and self-coupling on Ag/Cu/Cu_2O interfaces. In other words, *CO generated on Ag sites might spill over onto the Cu/Cu_2O interface to increase the surface coverage of *CO, thereby promoting C–C coupling toward C_2H_4 and retaining the balance with CO formation and consumption.[30,32] Furthermore, we characterized the three catalysts after the long-term CO_2RR test. The spent $Ag/Cu/Cu_2O_{Ag_{0.1}/HKUST\text{-}1}$ showed a well-retained phase composition (Ag/Cu/Cu_2O) in XRD (Fig. 4g). The HR-TEM images and the elemental mapping of $Ag/Cu/Cu_2O_{Ag_{0.1}/HKUST\text{-}1}$ clearly presented the interfaces of Ag/Cu/Cu_2O (Fig. S22, ESI†), indicating the good structural stability. By contrast, the Cu_2O(111) and (200) disappeared on the used $Cu/Cu_2O_{ER\text{-}HKUST\text{-}1}$, consistent with the drastic decrease of C_2H_4 FE. Accordingly, the AES results (Fig. 4h) identified the total disappearance of Cu(I) on $Cu/Cu_2O_{ER\text{-}HKUST\text{-}1}$, but the signal on $Ag/Cu/Cu_2O_{Ag_{0.1}/HKUST\text{-}1}$ was still visible after the CO_2RR, which confirmed the promoted stability of Cu(I) assisted by Ag additives. There are two related thermodynamic factors taken into consideration. First, the substantial disparity in the formation enthalpies of Cu_2O (−169 kJ mol^{-1}) and Ag_2O (−31.1 kJ mol^{-1}) suggests that any Ag oxide resulting from oxygen exposure will be rapidly reduced by the adjacent Cu.[32] Second, Ag, with its higher redox potential relative to Cu, can accept electrons from Cu. In addition, the negligible change of the Ag 3d signal in XPS further underscored the durability of the Ag/Cu/Cu_2O ternary interfaces in $Ag/Cu/Cu_2O_{Ag_{0.1}/HKUST\text{-}1}$ (Fig. S23, ESI†).

In further comparison with recently reported Cu-based electrocatalysts (Fig. 4i and Table S2, ESI†), $Ag/Cu/Cu_2O_{Ag_{0.1}/HKUST\text{-}1}$ presented an outstanding overall performance with excellent C_2H_4 FE, current output, and service life. Although some previous reports demonstrated the high FE of C_2H_4, they did not gain the high levels of current density and stability synchronously. For example, $CuPz_2$-Act-30 exhibited a high C_2H_4 FE of 67% in an H-cell, but the performance under high-current conditions such as in flow cells is still unclear.[20] S-HKUST-1 displayed a C_2H_4 FE of 57.2% at a current density of −400 mA cm^{-2} in a flow cell, but the stability test (480 min) was only conducted at −150 mA cm^{-2}.[18] Similarly, Cu–PzH yielded a C_2H_4 FE of 60% at −1.0 V (*vs.* RHE) with a large partial current density of 346.46 mA cm^{-2} while its stability remained for only 242 min.[59] More counterparts with rich Cu(I) species but prepared *via* other methods were further taken for comparison. For example, Cu_2O–BN and $Cu_2O@SiO_2$–NH_2 demonstrated stability exceeding 600 min,[61,64] whereas the C_2H_4 FEs of 35% and 15% were deemed suboptimal. An AgCu single-atom alloy blended with Ag nanoparticles showed a 94 ± 4% FE towards multi-carbon products at a high current density of ∼720 mA cm^{-2} in a flow cell, but the FE of C_2H_4 was below 40%.[42] In contrast, $Ag/Cu/Cu_2O_{Ag_{0.1}/HKUST\text{-}1}$ can achieve the superiority of C_2H_4 FE (∼50%), current output (>180 mA cm^{-2}), and stability (600 min) at the same time, underscoring its promise for practical use. When a membrane electrode assembly (MEA) reactor is rationally designed for such restructured catalysts, we believe greater advances in performance, in particular the greater current density and long-term stability, can be accomplished.[65]

In situ Raman spectra were obtained and the CO_2RR test was performed to understand the dynamic changes of the restructured interfaces. Different from $Cu_{HKUST\text{-}1}$, $Cu/Cu_2O_{ER\text{-}HKUST\text{-}1}$ and $Ag/Cu/Cu_2O_{Ag_{0.1}/HKUST\text{-}1}$ showed the band assigned to Cu(I) species at 520 and 610 cm^{-1} (Fig. 5a and b).[37] This band was well retained on $Ag/Cu/Cu_2O_{Ag_{0.1}/HKUST\text{-}1}$ for 300 min, while it became weaker and disappeared on $Cu/Cu_2O_{ER\text{-}HKUST\text{-}1}$. In the meantime, this evolution was confirmed by the *in situ* Raman spectra collected at various potentials (Fig. S24, ESI†). Such *in situ* monitoring, highly consistent with the post-CO_2RR AES analysis

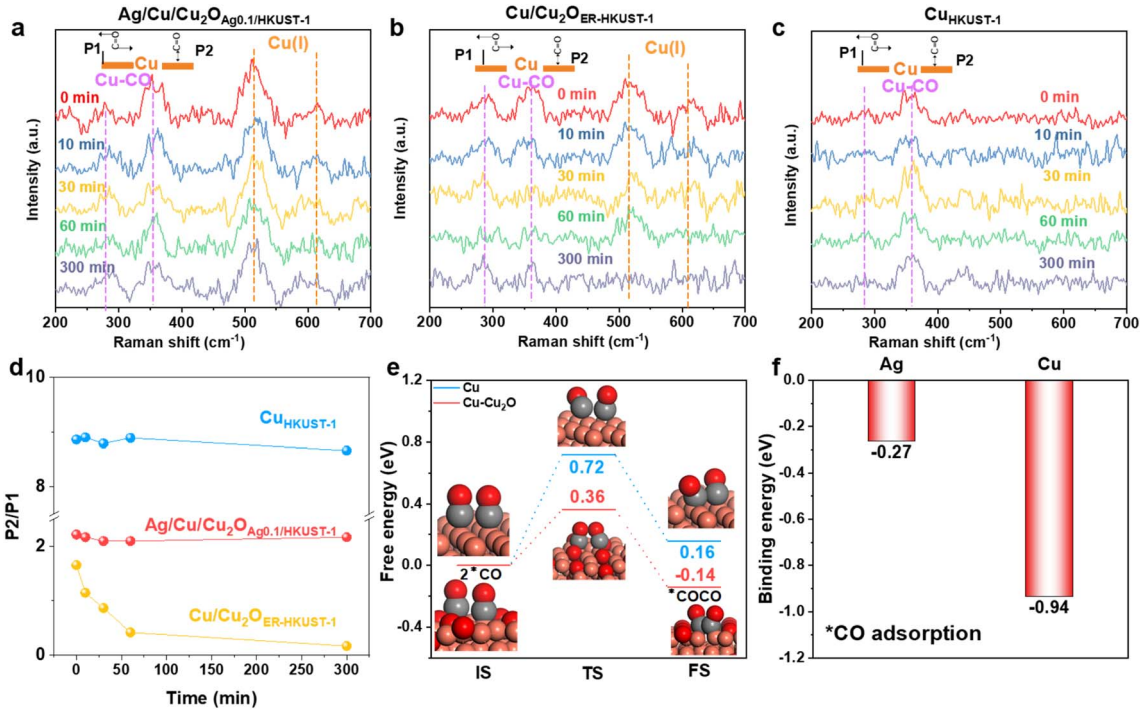

Fig. 5 *In situ* Raman spectra during the CO_2RR under different reaction times of (a) Ag/Cu/$Cu_2O_{Ag_{0.1}/HKUST-1}$, (b) Cu/$Cu_2O_{ER-HKUST-1}$ and (c) $Cu_{HKUST-1}$, and (d) the corresponding evolution of P2/P1 ratios. (e) Energy profiles for the initial states (ISs), transition states (TSs) and final states (FSs) of *CO–*CO coupling on Cu and Cu–Cu_2O models. (f) Energy profiles of *CO adsorption on Ag and Cu.

(Fig. 4h), identified again the stabilization of the Cu(I) species by Ag. Furthermore, the peaks at 280 and 364.3 cm^{-1}, corresponding to the restricted rotating (P1) and stretching (P2) models of adsorbed Cu–CO, respectively, could be detected on the surfaces, and the intensity ratio of P2/P1 peaks was a valid measure of the surface coverage of *CO.[36] The P2 band was the main peak while the P1 was very weak on $Cu_{HKUST-1}$ (Fig. 5c and d), and their large ratio of 8.5–9.0 indicated the extremely high *CO coverage on the Cu(0)-dominant surface,[66] consistent with the main distribution of CO in the products (Fig. 4d). In comparison with Cu/$Cu_2O_{ER-HKUST-1}$, Ag/Cu/$Cu_2O_{Ag_{0.1}/HKUST-1}$ delivered a larger P2/P1 ratio associated with the higher *CO coverage. More importantly, this ratio was kept at a high level above 2.0 on Ag/Cu/$Cu_2O_{Ag_{0.1}/HKUST-1}$ during the CO_2RR (0–300 min), but it drastically decreased on Cu/$Cu_2O_{ER-HKUST-1}$ (Fig. 5d). According to the recently evidenced tandem electrocatalysis on Ag/Cu interfaces,[67,68] we reasonably assumed that the CO spillover from Ag sites could increase the *CO coverage on Cu(0)–Cu(I) ensembles, leading to the well-maintained P2/P1 ratio on Ag/Cu/$Cu_2O_{Ag_{0.1}/HKUST-1}$ for the further C–C coupling.

To further understand the contribution of Ag and Cu_2O on the C–C coupling and ethylene production, the model structures of Cu and Cu–Cu_2O were taken for DFT calculations. As a critical step toward C_{2+} products, the coupling of two *CO was brought into focus. As shown in Fig. 5e, the kinetic barrier (0.36 eV) and enthalpy change (−0.14 eV) for the *CO coupling on Cu–Cu_2O are lower than those on Cu (0.72 and 0.16 eV), suggesting that the interfaces of Cu(0)–Cu(I) can effectively boost C_2 production. The coupling of two adjacent *CO on Cu–Ag should be difficult because of the high energy barrier (1.44 eV) (Fig. S25, ESI†), wherein the spillover of *CO from Ag to Cu would be preferred. Numerous studies have found that Ag has a high selectivity for CO in the CO_2RR which can provide adequate *CO for the tandem catalysis toward C_2 products.[30–32,67,68] As indicated by the more negative *CO binding energy on Cu (−0.94 eV) than that on Ag (−0.27 eV) (Fig. 5f), the spillover of the as-formed *CO from Ag to Cu and even Cu(0)–Cu(I) interfaces is thermodynamically favorable. Therefore, a tandem mechanism is proposed, in which the CO produced by Ag sites can diffuse to the reactive interface of Cu–Cu_2O with a low kinetic barrier for further coupling toward C_2H_4. In addition, Ag can stabilize the Cu(I) species to enable high ethylene production for a long time, which has been well validated by *in situ* Raman and *ex situ* XRD and AES.

Finally, we adopted other Cu-MOFs with the varied coordination as the pre-catalysts towards Ag/Cu/Cu_2O interfaces, to examine the applicability of this strategy. With a similar Cu–O_4 structure but a layered crystalline structure, CuBDC (BDC = 1,4-benzenedicarboxylic acid) underwent extensive reconstruction from 2D crystals to smaller nanoparticles, which was beneficial for restructuring Ag/Cu/Cu_2O interfaces when Ag was incorporated (Fig. S26, ESI†). Thanks to the rich interfaces of Ag/Cu/Cu_2O, the reconstructed samples afforded the obviously higher FE of C_2H_4 in comparison with that free from Ag. By contrast, $CuPz_2$ (Pz = pyrazol) with a Cu–N_4 structure cannot undergo the reconstruction under these working conditions due to the strong coordination of Cu–N_4 (Fig. S27, ESI†). When Ag was incorporated into $CuPz_2$, the resulting

samples unfortunately increased the FE of CO, probably due to the preferred generation of CO on the loaded Ag nanoparticles. The accordingly reduced FE of C_2H_4 also indicated the severely competitive reduction of CO_2 on Cu and Ag sites because of the absence of Ag/Cu interfaces. This is indirect proof for the tandem electrolysis towards C_2H_4 over Ag/Cu/$Cu_2O_{Ag_{0.1}/HKUST-1}$ *via* *CO spillover. It's clear that the coordination of Cu-based MOFs is important for restructuring Ag/Cu/Cu_2O interfaces, although the ligands make negligible influences on the electrocatalytic performance indeed because they have already been removed during the reconstruction (Fig. S11, ESI†). The frangible Cu–O_4 nodes are the prerequisite for the reconstruction, while the strong Cu–N_4 requires more tough conditions (*e.g.*, more negative potentials) to drive the reconfiguration.[20]

Conclusions

In summary, the directional *in situ* reconfiguration of Ag incorporating HKUST-1 frameworks was successfully introduced to restructure multi-phase Ag/Cu/Cu_2O electrocatalysts highly active for the CO_2RR. The reconstituted Ag/Cu/Cu_2O exhibited outstanding performance for the selective electroreduction of CO_2 to C_2H_4, with superior FE, current output, and service life to the most of recently reported counterparts. The combination of *in*/*ex situ* characterizations (Raman, XRD, XPS and AES) and theoretical calculations demonstrated that Ag plays a crucial role in stabilizing Cu(I) and increasing CO surface coverage, while the resulting Cu/Cu_2O interfaces significantly reduced the C–C coupling energy barrier toward the boosted ethylene production. This work not only offered a rational method to prepare highly active catalysts *via* electrochemical activation, but also deepened the understanding of the working state and mechanism on multi-phase interfaces. It's envisioned to gain further improvement *via* utilizing booming MOF pre-catalysts with more precise control over the coordination chemistry and dynamic evolution.

Data availability

Data supporting the findings of this study are available within the article ESI.†

Author contributions

Jiye Feng: synthesis, investigations, formal analysis, writing of the original draft, data curation. Wenbiao Zhang: DFT calculation, supervision. Danni Shi: experimental analysis, image polishing. Yingshuai Jia: proofreading of the original draft. Yi Tang: conceptualization, supervision, funding acquisition. Yuying Meng: conceptualization. Qingsheng Gao: conceptualization, supervision, writing – review and editing, funding acquisition.

Conflicts of interest

There are no conflicts to declare.

Acknowledgements

The authors appreciate the financial support from the National Natural Science Foundation of China (No. 22175077), Innovation Team Project in Guangdong Colleges and Universities (No. 2021KCXTD009), Guangdong Basic and Applied Basic Research Foundation (2023A1515240081), Guangzhou Science and Technology Program (No. 202201020071) and Fundamental Research Funds for the Central Universities (No. 21623103).

Notes and references

1 P. De Luna, C. Hahn, D. Higgins, S. A. Jaffer, T. F. Jaramillo and E. H. Sargent, *Science*, 2020, **367**, eaav3506.
2 D. Gao, R. M. Aran-Ais, H. S. Jeon and B. Roldan Cuenya, *Nat. Catal.*, 2019, **2**, 198–210.
3 T. Yan, X. Chen, L. Kumari, *et al.*, *Chem. Rev.*, 2023, **123**, 10530–10583.
4 M. Kuang and G. Zheng, *Chem Catal.*, 2023, **3**, 100565.
5 Q. Chen, X. Wang, Y. Zhou, Y. Tan, H. Li, J. Fu and M. Liu, *Adv. Mater.*, 2024, **36**, 2303902.
6 S. Nitopi, E. Bertheussen, S. B. Scott, *et al.*, *Chem. Rev.*, 2019, **119**, 7610–7672.
7 M. G. Kibria, J. P. Edwards, C. M. Gabardo, D. Cao-Thang, A. Seifitokaldani, D. Sinton and E. H. Sargent, *Adv. Mater.*, 2019, **31**, 1807166.
8 B. Chang, H. Pang, F. Raziq, S. Wang, K.-W. Huang, J. Ye and H. Zhang, *Energy Environ. Sci.*, 2023, **16**, 4714–4758.
9 H. Yang, S. Li and Q. Xu, *Chin. J. Catal.*, 2023, **48**, 32–65.
10 R. M. Aran-Ais, F. Scholten, S. Kunze, R. Rizo and B. Roldan Cuenya, *Nat. Energy*, 2020, **5**, 317–325.
11 C. Xiao and J. Zhang, *ACS Nano*, 2021, **15**, 7975–8000.
12 Q. J. Wu, J. Liang, Y. B. Huang and R. Cao, *Acc. Chem. Res.*, 2022, **55**, 2978–2997.
13 H. L. Zhu, J. R. Huang, P. Q. Liao and X. M. Chen, *ACS Cent. Sci.*, 2022, **8**, 1506–1517.
14 X. Kang, Q. Zhu, X. Sun, J. Hu, J. Zhang, Z. Liu and B. Han, *Chem. Sci.*, 2016, **7**, 266–273.
15 D. Yao, C. Tang, A. Vasileff, X. Zhi, Y. Jiao and S.-Z. Qiao, *Angew. Chem., Int. Ed.*, 2021, **60**, 18178–18184.
16 X. Xie, X. Zhang, M. Xie, *et al.*, *Nat. Commun.*, 2022, **13**, 63.
17 J. D. Yi, R. Xie, Z. L. Xie, G. L. Chai, T. F. Liu, R. P. Chen, Y. B. Huang and R. Cao, *Angew. Chem., Int. Ed.*, 2020, **59**, 23641–23648.
18 C. F. Wen, M. Zhou, P. F. Liu, *et al.*, *Angew. Chem., Int. Ed.*, 2022, **61**, e202111700.
19 W. Zhang, C. Huang, J. Zhu, *et al.*, *Angew. Chem., Int. Ed.*, 2022, **61**, e202112116.
20 C. Liu, X.-D. Zhang, J.-M. Huang, M.-X. Guan, M. Xu and Z.-Y. Gu, *ACS Catal.*, 2022, **12**, 15230–15240.
21 J. Cheng, L. Chen, X. Xie, *et al.*, *Angew. Chem., Int. Ed.*, 2023, **62**, e202312113.
22 J.-X. Wu, S.-Z. Hou, X.-D. Zhang, M. Xu, H.-F. Yang, P.-S. Cao and Z.-Y. Gu, *Chem. Sci.*, 2019, **10**, 2199–2205.
23 J.-Y. Kim, D. Hong, J.-C. Lee, *et al.*, *Nat. Commun.*, 2021, **12**, 3765.

24 C. Hahn, T. Hatsukade, Y.-G. Kim, A. Vailionis, J. H. Baricuatro, D. C. Higgins, S. A. Nitopi, M. P. Soriaga and T. F. Jaramillo, *Proc. Natl. Acad. Sci. U. S. A.*, 2017, **114**, 5918–5923.
25 D. Wakerley, S. Lamaison, J. Wicks, *et al.*, *Nat. Energy*, 2022, **7**, 130–143.
26 X.-D. Zhang, T. Liu, C. Liu, *et al.*, *J. Am. Chem. Soc.*, 2023, **145**, 2195–2206.
27 S.-C. Lin, C.-C. Chang, S.-Y. Chiu, H.-T. Pai, T.-Y. Liao, C.-S. Hsu, W.-H. Chiang, M.-K. Tsai and H. M. Chen, *Nat. Commun.*, 2020, **11**, 3525.
28 W. Zhang, Y. Yang, Y. Tang and Q. Gao, *J. Energy Chem.*, 2022, **70**, 414–436.
29 C.-J. Chang, S.-C. Lin, H.-C. Chen, J. Wang, K. J. Zheng, Y. Zhu and H. M. Chen, *J. Am. Chem. Soc.*, 2020, **142**, 12119–12132.
30 C. Chen, Y. Li, S. Yu, S. Louisia, J. Jin, M. Li, M. B. Ross and P. Yang, *Joule*, 2020, **4**, 1688–1699.
31 T. Yang, M. Kuang and J. Yang, *Nano Res.*, 2023, **16**, 8670–8683.
32 T. T. H. Hoang, S. Verma, S. Ma, T. T. Fister, J. Timoshenko, A. I. Frenkel, P. J. A. Kenis and A. A. Gewirth, *J. Am. Chem. Soc.*, 2018, **140**, 5791–5797.
33 Z. Song, Y. Liu, Y. Zhong, Q. Guo, J. Zeng and Z. Geng, *Adv. Mater.*, 2022, **34**, 2204306.
34 H. Sun, X. Han, K. Liu, B. Shen, J. Liu, D. Wu and X. Shi, *Ind. Eng. Chem. Res.*, 2017, **56**, 9541–9550.
35 N. Dae-Hyun, O. S. Bushuyev, J. Li, *et al.*, *J. Am. Chem. Soc.*, 2018, **140**, 11378–11386.
36 C. Zhan, F. Dattila, C. Rettenmaier, A. Bergmann, S. Kuhl, R. Garcia-Muelas, N. Lopez and B. R. Cuenya, *ACS Catal.*, 2021, **11**, 7694–7701.
37 S. Mu, H. Lu, Q. Wu, L. Li, R. Zhao, C. Long and C. Cui, *Nat. Commun.*, 2022, **13**, 3694.
38 Y. Lin, T. Wang, L. Zhang, *et al.*, *Nat. Commun.*, 2023, **14**, 3575.
39 Y. Wu, J. Feng, D. Shi, W. Zhang, Y. Tang and Q. Gao, *Chem. Commun.*, 2023, **59**, 10428–10431.
40 Y. Guo, C. Feng, S. Wang, *et al.*, *J. Mater. Chem. A*, 2020, **8**, 24477–24485.
41 I. Lopez-Salido, D. C. Lim and Y. D. Kim, *Surf. Sci.*, 2005, **588**, 6–18.
42 C. Du, J. P. Mills, A. G. Yohannes, *et al.*, *Nat. Commun.*, 2023, **14**, 6142.
43 M. Luo, Z. Wang, Y. C. Li, *et al.*, *Nat. Commun.*, 2019, **10**, 5814.
44 Z. Weng, J. Jiang, Y. Wu, *et al.*, *J. Am. Chem. Soc.*, 2016, **138**, 8076–8079.
45 S. Kusama, T. Saito, H. Hashiba, A. Sakai and S. Yotsuhashi, *ACS Catal.*, 2017, **7**, 8382–8385.
46 Y.-S. Cheng, X.-P. Chu, M. Ling, N. Li, K.-L. Wu, F.-H. Wu, H. Li, G. Yuan and X.-W. Wei, *Catal. Sci. Technol.*, 2019, **9**, 5668–5675.
47 F. Yang, A. Chen, P. L. Deng, Y. Zhou, Z. Shahid, H. Liu and B. Y. Xia, *Chem. Sci.*, 2019, **10**, 7975–7981.
48 A. Guan, Z. Chen, Y. Quan, *et al.*, *ACS Energy Lett.*, 2020, **5**, 1044–1053.
49 J.-D. Yi, R. Xie, Z.-L. Xie, G.-L. Chai, T.-F. Liu, R.-P. Chen, Y.-B. Huang and R. Cao, *Angew. Chem., Int. Ed.*, 2020, **59**, 23641–23648.
50 Y. Zhou, S. Chen, S. Xi, Z. Wang, P. Deng, F. Yang, Y. Han, Y. Pang and B. Y. Xia, *Cell Rep. Phys. Sci.*, 2020, **1**, 100182.
51 H. Huo, J. Wang, Q. Fan, Y. Hu and J. Yang, *Adv. Energy Mater.*, 2021, **11**, 2102447.
52 X.-F. Qiu, H.-L. Zhu, J.-R. Huang, P.-Q. Liao and X.-M. Chen, *J. Am. Chem. Soc.*, 2021, **143**, 7242–7246.
53 L. Zhang, X.-X. Li, Z.-L. Lang, *et al.*, *J. Am. Chem. Soc.*, 2021, **143**, 3808–3816.
54 Y. Zhang, L.-Z. Dong, S. Li, X. Huang, J.-N. Chang, J.-H. Wang, J. Zhou, S.-L. Li and Y.-Q. Lan, *Nat. Commun.*, 2021, **12**, 6390.
55 R. Chen, L. Cheng, J. Liu, Y. Wang, W. Ge, C. Xiao, H. Jiang, Y. Li and C. Li, *Small*, 2022, **18**, 2200720.
56 D.-S. Huang, H.-L. Zhu, Z.-H. Zhao, J.-R. Huang, P.-Q. Liao and X.-M. Chen, *ACS Catal.*, 2022, **12**, 8444–8450.
57 L.-L. Zhuo, P. Chen, K. Zheng, *et al.*, *Angew. Chem., Int. Ed.*, 2022, **61**, e202204967.
58 B. Kim, Y. C. Tan, Y. Ryu, *et al.*, *ACS Energy Lett.*, 2023, **8**, 3356–3364.
59 R. Wang, J. Liu, Q. Huang, *et al.*, *Angew. Chem., Int. Ed.*, 2021, **60**, 19829–19835.
60 P. P. Guo, Z. H. He, S. Y. Yang, W. T. Wang, K. Wang, C. C. Li, Y. Y. Wei, Z. T. Liu and B. X. Han, *Green Chem.*, 2022, **24**, 1527–1533.
61 Y. Zhou, Y. Yao, R. Zhao, *et al.*, *Angew. Chem., Int. Ed.*, 2022, **134**, e202205832.
62 X. Ma, X. Song, L. Zhang, *et al.*, *Green Chem.*, 2023, **25**, 7635–7641.
63 F. Yu, X. Liu, L. Liao, G. Xia and H. Wang, *Small*, 2023, **19**, 2301558.
64 Z.-Y. Zhang, H. Tian, H. Jiao, X. Wang, L. Bian, Y. Liu, N. Khaorapapong, Y. Yamauchi and Z.-L. Wang, *J. Mater. Chem. A*, 2024, **12**, 1218–1232.
65 Y. Liang, J. Zhao, Y. Yang, *et al.*, *Nat. Commun.*, 2023, **14**, 474.
66 T.-C. Chou, C.-C. Chang, H.-L. Yu, *et al.*, *J. Am. Chem. Soc.*, 2020, **142**, 2857–2867.
67 J. Huang, M. Mensi, E. Oveisi, V. Mantella and R. Buonsanti, *J. Am. Chem. Soc.*, 2019, **141**, 2490–2499.
68 Y. Yu, D. Wang, Y. Hong, T. Zhang, C. Liu, J. Chen, G. Qin and S. Li, *Chem. Commun.*, 2022, **58**, 11163–11166.